Optics Communications 426 (2018) 142–150

Contents lists available at ScienceDirect

Optics Communications

journal homepage: www.elsevier.com/locate/optcom

Laboratory radiometric calibration of the channeled interference imaging spectropolarimeter

Qiwei Li [a,*], Chunmin Zhang [b,c], Fang Lu [a], Changjiang Zhu [a]

[a] School of Physics and Optoelectronic Engineering, Xidian University, Xi'an 710071, China
[b] School of Science, Xi'an Jiaotong University, Xi'an 710049, China
[c] Institute of Space Optics, Xi'an Jiaotong University, Xi'an 710049, China

ARTICLE INFO

Keywords:
Radiometric calibration
Channeled interference imaging spectropolarimeter
Interference fringe
Least square method

ABSTRACT

The radiometric calibration is the prerequisite and guarantee for realizing quantitative detection of the spectral characteristics for the channeled interference imaging spectropolarimeter (CIISP). A complete set of experimental scheme and processing algorithm of the lab radiometric calibration for CIISP were detailed presented. In relative radiometric calibration, the dark current noise of the CIISP was eliminated firstly, and then the uniformity correction was implemented according to the characteristics of the output interferogram formed by CIISP. The response uniformity of pixels in CCD detector was efficiently improved, as well as the vignetting effects of the instrument. By the absolute radiometric calibration, the spectral responsivity was corrected at each wavelength, and the functional relation between the standard spectral radiance and the dimensionless reconstructed spectral data was established. As a result, the maximum root-mean-square error of the calibrated spectrum was approximate 1.88% within the wavebands which have a normal signal-to-noise ratio. The study provides us a quite efficient and high-precision calibration method that is well applicable to other detection modes of the CIISP.

1. Introduction

Imaging spectropolarimeter is a versatile instrument which combines the abilities of an imaging spectrometer and imaging polarimeter to provide a full four-dimensional (two spatial, one spectral, one polarization) datacube [1]. It improves the ability of object detection with preferable accuracy, and has been recognized as a powerful tool in many fields, such as remote sensing, environmental monitoring, biomedical diagnosis, and other scientific areas [2–6].

The channeled polarimetric technique, first implemented by Oka and Kato, is an attractive approach for spectropolarimetry [7]. It is efficiently combined with the Fourier transform spectrometers which exploit interferometric techniques, and creates a channeled interference imaging spectropolarimeter (CIISP). The CIISP has become a hot research topic since it maintains the throughput (Jacquinot) and multiplex (Fellgett) advantages compared to the dispersive spectrometry [8]. In addition, it can capture the image, spectrum and polarization state of target simultaneously without internal moving parts, electrically controllable or micro components, which brings the advantages of static state, high optical throughput, and easy alignment.

According to different ways of producing optical path differences for CIISP, it can be classified as temporally-modulated [9,10], spatially-modulated [11], and spatio-temporally modulated mode, respectively [12,13]. The spatio-temporally modulated detection mode is newly developed for CIISP, which is based on the lateral shearing interferometer and uses a large aperture field stop to replace the entrance slit, thus offers a large optical throughput as well as a static and compact structure. However, in development of such instrument, the original reconstructed spectral data can only roughly reflect the radiant and spectral characteristics of the object, which is due to the influences of many factors in the process of optical manufacture and alignment, such as the dark current noise, non-uniformity response of the system, uneven distribution of the interferogram fringes and so on. In order to improve the detecting precision of the CIISP, and more truly describe the physicochemical property of the object [14], high-precision and efficient radiometric calibration for the instrument is necessary.

In this paper, we first briefly recall the principle of CIISP based on spatio-temporally modulated mode. Then a complete set of experimental scheme and processing procedure of the lab radiometric calibration for CIISP are detailed presented for the first time, as well as the calibration

* Corresponding author.
E-mail address: lqw17@xidian.edu.cn (Q. Li).

https://doi.org/10.1016/j.optcom.2018.05.033
Received 30 March 2018; Received in revised form 7 May 2018; Accepted 9 May 2018
Available online 26 May 2018

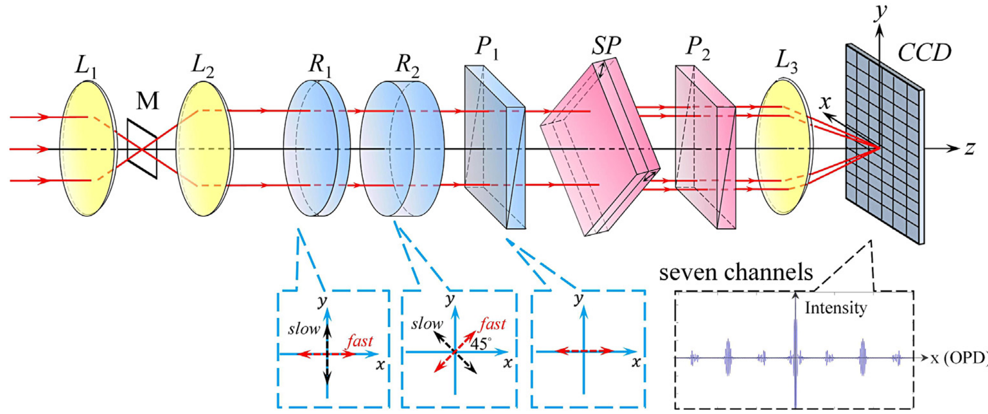

Fig. 1. Optical layout of CIISP based on Savart polariscope.

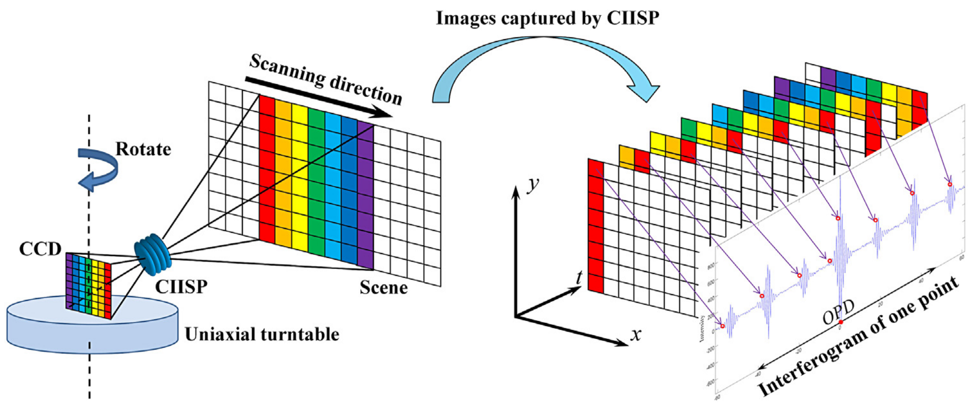

Fig. 2. Data acquisition model of the CIISP system.

result of each process. The calibration procedures are quite efficient and general that can be applicable to other detection modes of CIISP such as the temporally-modulated and spatially-modulated modes.

2. Brief principle of the CIISP

The principle of channeled interference imaging spectropolarimetry has already been presented in Refs. [8,10]. Here, a short description of the configuration of the CIISP based on Savart polariscope is given, as shown in Fig. 1. Light from the scene is imaged on intermediate image plane M by lens L_1 and then collimated by lens L_2. The parallel light passes through two high-order birefringent retarders, R_1, R_2, and an analyzer P_1, which becomes linearly polarized at 0° to the x axis. By the Savart polariscope (SP) interferometer [15–17], the incoming light is parallel laterally sheared into a pair of equal-amplitude but orthogonally polarized components. After passing through P_2, the identical linearly polarized components are extracted and recombined onto the CCD detector by imaging lens L_3.

The imaging system superimposes the channeled interference fringes on the scene, which leads to an intensity-modulated image. The fringe pattern is straight bright–dark lines that parallel to the y-axis. Note that the typical interference fringes usually consist of seven channels separated in optical path difference (OPD) dimension, and the spectral and polarized information can be obtained by filtering part of the channels and followed by a fast Fourier transform (FFT).

The CIISP can be equipped on aircraft or ground equipment such as translation stage and turntable, as shown in Fig. 2. It moves over the whole area, every plot of the scene experiences the process that the incident angle changes from maximum, zero, finally to negative maximum [18]. At the same time, the CCD detector records a full two-dimensional image per frame, with successive frames associated with different OPD by scanning across a scene. Thereby, the full interferometric data of a target have to be picked out from a series CCD images respectively and organize them regularly. We have developed a CIISP prototype with independent intellectual property rights, and its working spectral range is from 480 nm to 960 nm. The detector is a 12bit monochrome CCD with the resolution of 512×512, and the maximum frame rate can reach to 300 Hz. The number of sampling point is 512 for a two-sided interferogram, and the sampling interval of the OPD is 0.24 μm.

3. Radiometric calibration

Laboratory radiometric calibration should be implemented for CIISP in order to reconstruct accurate spectropolarimetric information from the original interferogram images. It was performed through two fundamental processes, namely relative and absolute radiometric calibration according to the principle and characteristics of the CIISP. The specific calibration flow chart is shown in Fig. 3, and each calibration sub-process will be discussed in detail in following sections.

3.1. Relative radiometric calibration

The non-uniformity response of CIISP caused by vignetting artifacts, uneven transmittance of the optical elements, and CCD detector manufacturing defects will lead to striping and banding in the image. In order to reconstruct the correct spectropolarimetric information from the scene without including background effects, detector offsets must be accounted for via a relative radiometric calibration of the sensor.

(1) Dark current removal

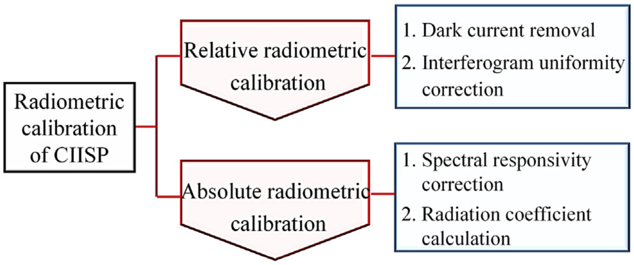

Fig. 3. Lab radiometric calibration flow chart.

The dark current (DC) of a CCD detector refers to the output value of the optical signal receiving unit in a no-light environment when the CCD operates normally. It can be treated as background noises which should be eliminated before information reconstruction. We recorded the DC by wrapping up the instrument with black velvet, and the lens cap of the instrument was covered. The dark current images of the CCD detector were collected with ten non-interval exposure times of 5 ms, 10 ms, 20 ms, 40 ms, 50 ms, 80 ms, 100 ms, 200 ms, 400 ms, 500 ms respectively, which cover the typical acquisition time per frame of CIISP. Note that at least 20 images was recorded in each exposure time and taken a weighted average to reduce random errors.

Fig. 4(a) shows the DC images with sequential exposure time. It can be seen that the CCD detector consists of 16 small light-sensitive areas with uneven DC distribution. The gain factor in lower half of plane array is higher than upper half, and the DC of pixels in junctures is lower than other areas. Fig. 4(b) displays the digital number (DN) value of dark current in column 220 and row 220 of the images respectively with increasing exposure time.

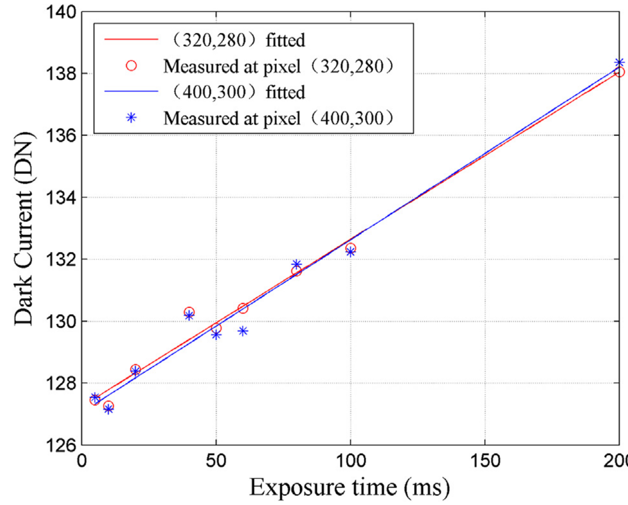

Fig. 5. Linear fitting curve of the dark current changing with the exposure time.

For different exposure times $T^m (1 \leq m \leq 10)$, the dark current $D_{i,j}^m$ of each pixel (i, j) in CCD detector can be assumed as

$$\begin{bmatrix} D_{i,j}^1 \\ D_{i,j}^2 \\ \vdots \\ D_{i,j}^m \end{bmatrix} = \begin{bmatrix} T^1 & 1 \\ T^2 & 1 \\ \vdots & \vdots \\ T^m & 1 \end{bmatrix} \begin{bmatrix} k_{i,j} \\ b_{i,j} \end{bmatrix} \tag{1}$$

where $k_{i,j}$ and $b_{i,j}$ are the fitting coefficients of each pixel which can be obtained by using the least-squares method. Fig. 5 shows the fitted result of two arbitrarily selected pixels. It can be seen that the DC value is changed linearly and slowly with different exposure times. Therefore,

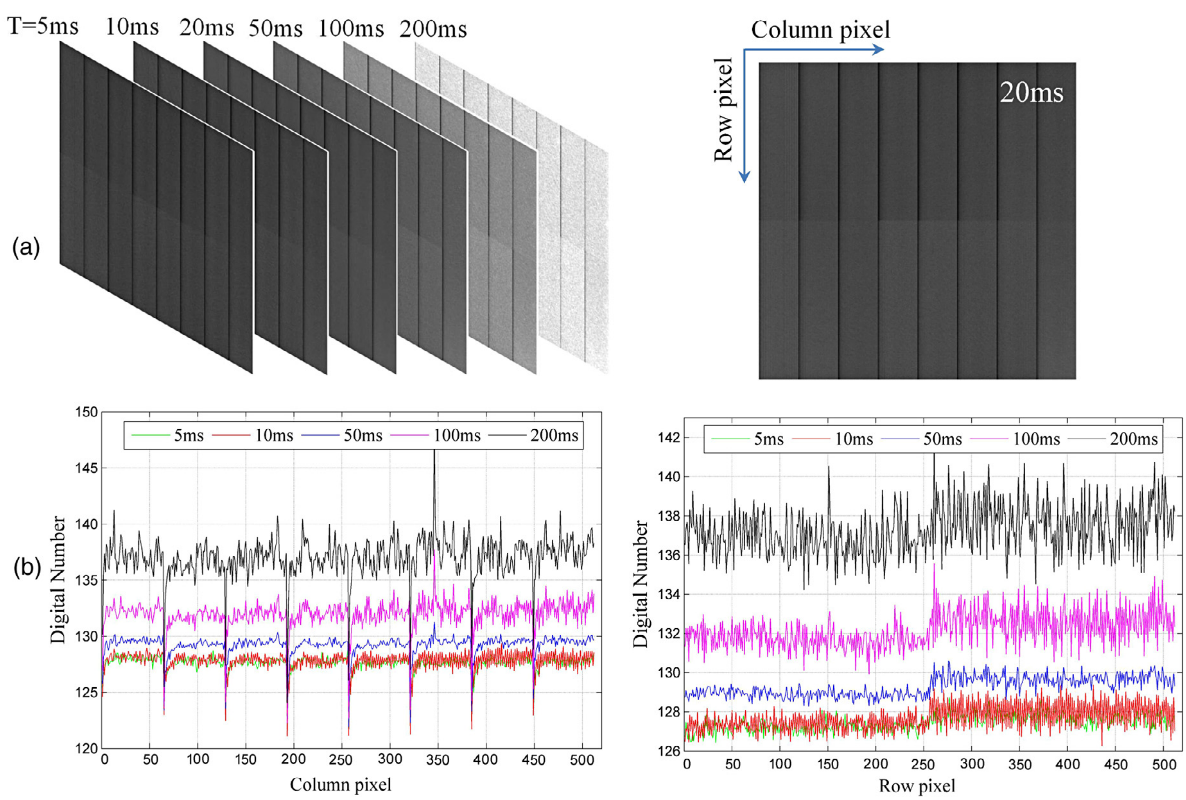

Fig. 4. (a) The dark current images with incremental exposure times. (b) The dark current value of pixels in row 200 and column 200, respectively.

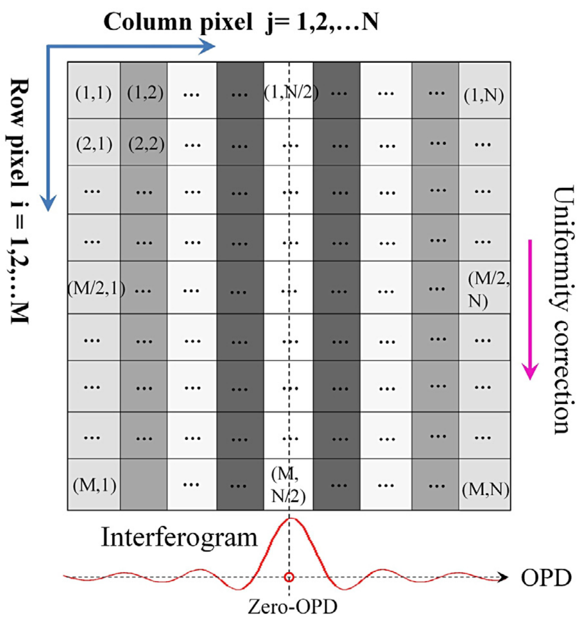

Fig. 6. The uniformity correction principle for the interferogram image.

sometimes in order to shorten the calibration time, we can directly subtract the dark current collected in calibration experiment instead of the actually calculated ones with the closest timestamp.

(2) Interferogram uniformity correction

The interferogram uniformity correction for the CIISP is also called the flat-field, which refers to the non-uniform correction for the detector unit response and uneven system energy transmission. However, the traditional method of flat-field for CCD detector cannot be directly applied for CIISP, because the channeled interference fringes are superimposed on image plane, which leads to a rapidly changed DN values and cannot be efficiently removed. Fortunately, the fringe pattern of the CIISP is similar to that in the Young's double slit setup and is straight line which parallels to the vertical direction. Therefore, the pixels in the same column (vertical direction) should have identical DN values if the object has homogeneous luminosity and chroma, because these pixels are located in the same OPD. According to the properties of the output interferogram, the uniformity correction can be performed along the direction of the interference fringes, rather than the whole CCD image, as shown in Fig. 6.

(A) Choice of calibration light source

The calibration light source should first be considered before performing the flat-field. A broadband unpolarized light with steady uniform radiation is the optimal calibration source for CIISP for the following reasons.

The feature of steady uniform radiation is the basic requirement for interferogram uniformity correction described above, and it can also simplify the whole calibration experiment. Because the multifarious scanning operation of the CIISP described above can be omitted if the scene provides homogeneous radiation, and a single frame image is enough for interferogram acquisition and information reconstruction.

For the restriction of detecting principle, a narrowband polarized light will lead to obvious aliasing errors in interferogram as can be

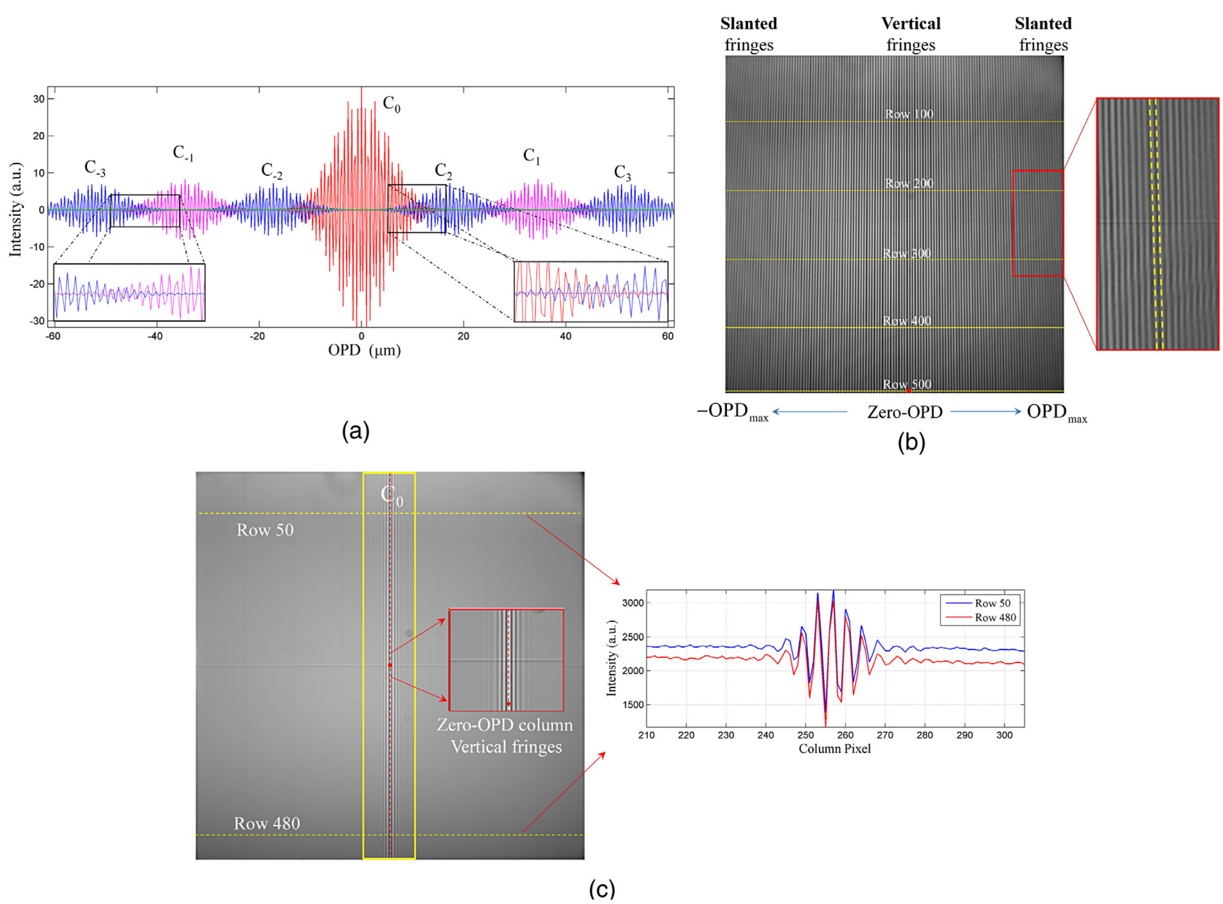

Fig. 7. (a) Simulated interferogram of the CIISP for a linearly polarized narrowband light source, and the full width at half maximum of spectrum is about 25 nm. (b) Interferogram image formed by a monochromatic light, and the fringes gradually tilted in big OPD areas. (c) Interferogram image formed by broadband unpolarized light, the maximum deviation of the fringes between row 50 and row 480 is less than one pixel.

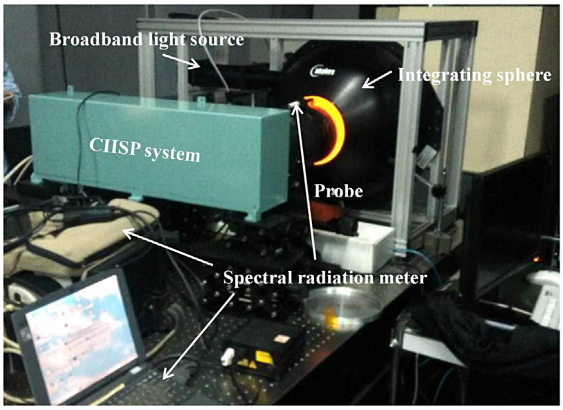

Fig. 8. The data collection of interferogram uniformity correction.

seen in Fig. 7(a) [19], and this can be reduced or even eliminated by using broadband light. Because the modulation of the fringes in each interferometric channel (e.g. $C_0, \pm C_1, \pm C_2, \pm C_3$) decreased rapidly with increasing spectral bandwidth, and the crosstalk between adjacent channels will be minimized. On the other hand, the collected interferogram images formed by the broadband light which covers the spectral range of CIISP can be directly used in the later procedure of radiation coefficient calculation.

Another problem needs to be solved is the slant of fringes as shown in Fig. 7(b). It is caused by the Savart interferometer which introduces non-ignorable quadratic OPD at a large incident angle ($> 3°$) [20,21]. As seen, the fringe patterns are vertical near zero-OPD areas, but sloping gradually towards large-OPD areas, hence the uniformity correction performed along the column is no longer applicable. Fortunately, this can be solved by using unpolarized white light. Because the channels located at large-OPD areas contains only polarized information. Therefore, the fringes in channels of $\pm C_1, \pm C_2, \pm C_3$ will disappear (C_0 channel with vertical fringes is still exist), and the areas only remain the uniform background (image of the scene) if the unpolarized white light can be used. It can be seen clearly in Fig. 7(c), the positions (horizontal axis) of the crests and troughs of the interference fringes are approximately overlap each other, and the maximum deviation of fringes between row 50 and row 480 is less than one pixel. Therefore, the uniformity correction errors caused by slant fringes can be ignored.

(B) Experiment and calibration result

The experimental setup for interferogram uniformity correction is shown in Fig. 8. A uniform light source integrating sphere (Labsphere XTH2000) was used to generate the broadband unpolarized light, which was placed sufficiently close to the CIISP such as to fill the entrance pupil. The built-in light source consists of a standard xenon and halogen tungsten lamp. The actual measured degree of polarization (DoP) of the output light with different wavelengths (e.g. 500, 633, 700, and 900 nm, respectively) is less than 0.1%, which can be considered as an ideal unpolarized source, and the radiance uniformity is better than 98%. The radiant brightness of the integrating sphere can be adjusted continuously by controlling the apertures of multiple external sources and the electrical current of internal sources. A spectral radiation meter, with the national measurement standard as a standard transmission, was placed next to the CIISP and used to monitor and record different radiant brightness levels for the calibration.

Ten sets of radiance data with exposure time from 5 ms to 500 ms (the same as in dark current removal procedure) were collected by CIISP and the spectral radiation meter respectively. At each exposure time, sixteen DN values of the 12bit CCD were recorded from 1000 to 4000 in increments of 200, which cover the scope of the gray level. Ten images were recorded in each gray level and taken a weighted average. Note that the test variation is based on the DN value of the center bright zero-order fringe.

The DN value of the original interferogram images should be subtracted by the dark current and given as $DN_{i,j}^t(L)$. According to the principle of the interferogram uniformity correction, the calibration coefficient $G_{i,j}^t$ can be expressed as

$$G_{i,j}^t(L) = \frac{\overline{DN_j^t}(L)}{DN_{0_{i,j}}^t(L) - D_{i,j}^t} \tag{2}$$

where $DN_{0_{i,j}}^t(L)$ is the original DN of (i,j) pixel in radiance value L with exposure time of t; $D_{i,j}^t$ is the CCD dark current calculated via Eq. (1); $\overline{DN_i^t}(L)$ is the desired output DN value, and is equal to the average DN value of the pixels in jth column. The least square fit was employed to establish the relationship between $G_{i,j}^t$ and $DN_{i,j}^t$ through $n(1 \le n \le 16)$ radiance values. Here the linear fitting was selected and given in Eq. (3) since the pixels have good linear response.

$$\begin{bmatrix} {}^1G_{i,j}^t \\ {}^2G_{i,j}^t \\ \vdots \\ {}^nG_{i,j}^t \end{bmatrix} = \begin{bmatrix} {}^1DN_{i,j}^t & 1 \\ {}^2DN_{i,j}^t & 1 \\ \vdots & \vdots \\ {}^nDN_{i,j}^t & 1 \end{bmatrix} \begin{bmatrix} R_{i,j}^t \\ O_{i,j}^t \end{bmatrix} \tag{3}$$

The coefficients of the linear equation can be obtained and each pixel corresponds to a set of $R_{i,j}^t$ and $O_{i,j}^t$. Hence, the corrected DN value of each pixel can be acquired by multiplying the corresponding coefficient into the DN values for the uncorrected image, as can be seen in Fig. 9.

Fig. 10 depicts the DN value of an arbitrarily selected row and column pixels from the two images above. In Fig. 10(a), the DN values of pixels in the same column are within a large range from 2085 to 2298 in original data, which reduced to the scope of 2188–2218 after calibration. Fig. 10(b) shows that the interferogram becomes more symmetrical after calibration, and the step changes of DN value caused by CCD light-sensitive component junctures are corrected as well. Fig. 11 depicts the response linearity of six pixels in one column. The response curves which using 15 incremental radiance points shows good linearity of each pixel. The straight lines in Fig. 11(b) approximately overlap each other after calibration, which indicates the obvious non-uniformity existing in original data has been well calibrated.

3.2. Absolute radiometric calibration

(1) Spectral responsivity correction

The transmittance of optical elements and the spectral responsivity of CCD detector vary with the wavelengths within the detecting spectral range, hence the spectral responsivity of CIISP should be determined through spectral responsivity correction. It was performed using a combination of the monochromator and integrating sphere as the light source to generate unpolarized monochromatic light with uniform radiation as shown in Fig. 12(a). The output wavelengths of monochromator were selected every 5 nm within the detecting spectral range. The probe of the spectral radiation meter was placed next to the device recording the radiance (L) with CIISP simultaneously. The interferogram images were collected and averaged over 10 sequential measurements.

The normalized spectral responsivity of CIISP can be acquired from the DN value of the interferogram images and the measured radiance, as shown in Fig. 12(b). The high-order polynomial curve fitting was used to smooth the measurement data. It can be seen that the spectral responsivity varies obviously with wavelength change, especially at the edges of the spectral bands. The value of normalized spectral responsivity is less than 0.5 within the spectral bands of 480–510 nm and 910–960 nm, which means the interferometric data may have a relatively low signal-to-noise ratio formed by these bands.

(2) Radiation coefficient calculation

As a last step, radiation coefficient calculation was introduced to establish the functional relation between the standard spectral radiance and the dimensionless reconstructed spectral data of CIISP.

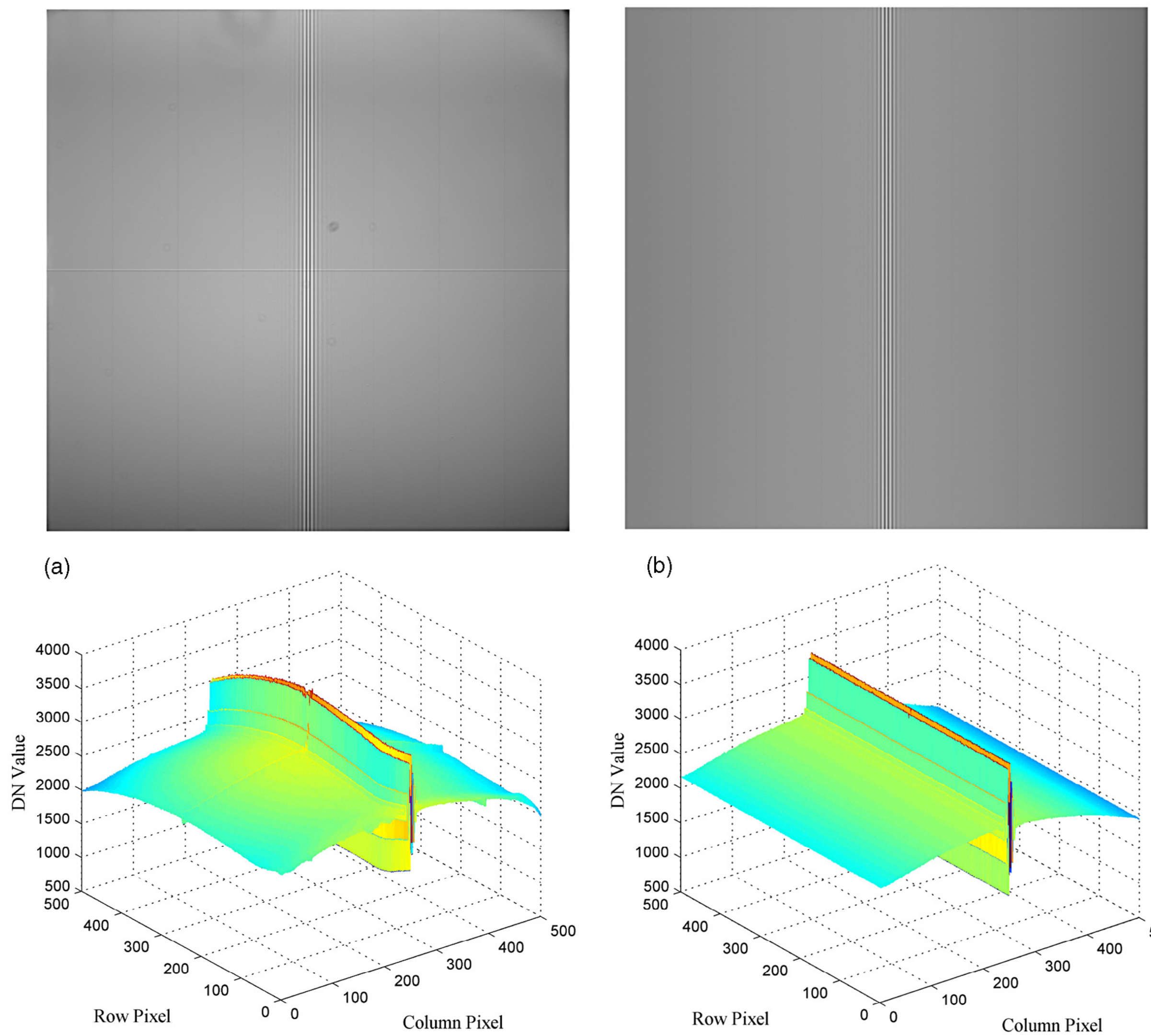

Fig. 9. (a) The interferogram image and its DN values of an unpolarized broadband light with exposure time of 10 ms, the dark current has been removed in the first step. (b) The interferogram data after relative radiometric calibration, the non-uniformity of the CIISP has been well improved.

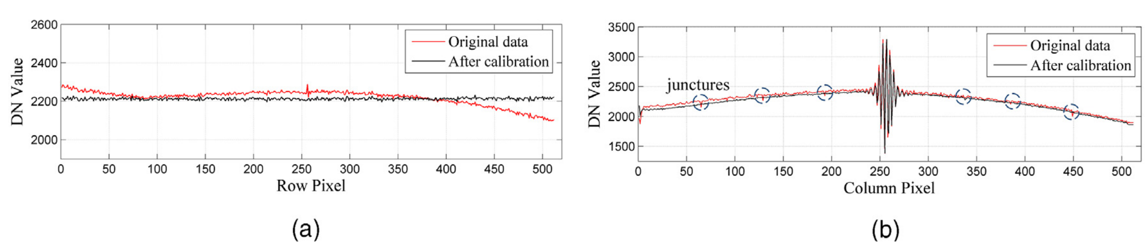

Fig. 10. The DN value of the pixels in column 240 (a) and row 220 (b) from the two images.

In process of interferogram uniformity correction (in Section 3.1), a series of interferogram images with $n(1 \leq n \leq 16)$ incremental spectral radiances, which cover the scope of gray level of the CCD detector, were collected by the CIISP, and each spectral radiance was recorded by the spectral radiation meter simultaneously. The spectrum of the incident light can be reconstructed from the interferograms after performing ordinal calibration procedures above. While the reconstructed spectral data M_k in waveband λ_k, is a dimensionless number (DN value) as shown in Fig. 14(b). The relationship between M_k and the actual measured spectral radiance can be given as

$$\begin{bmatrix} {}^{1}L_k^t \\ {}^{2}L_k^t \\ \vdots \\ {}^{n}L_k^t \end{bmatrix} = \begin{bmatrix} {}^{1}M_k^t & 1 \\ {}^{2}M_k^t & 1 \\ \vdots & \vdots \\ {}^{n}M_k^t & 1 \end{bmatrix} \begin{bmatrix} E_k^t \\ F_k^t \end{bmatrix} \tag{4}$$

where L_k^t is the standard spectral radiances in waveband λ_k with exposure time of t; E_k^t and F_k^t are the linear fitting coefficients and determined for each waveband. Fig. 13 depicts the fitted result of selected bands within the detecting spectral range, which is produced using 15 incremental radiance points. The fitted line coincides perfectly with the

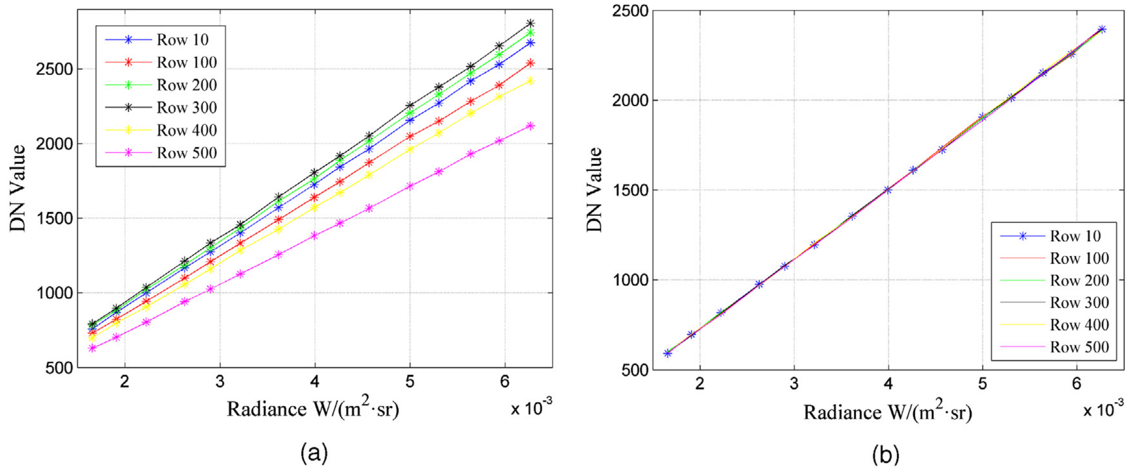

Fig. 11. The response linearity of 6 pixels in column 240 between original data (a) and calibrated data (b).

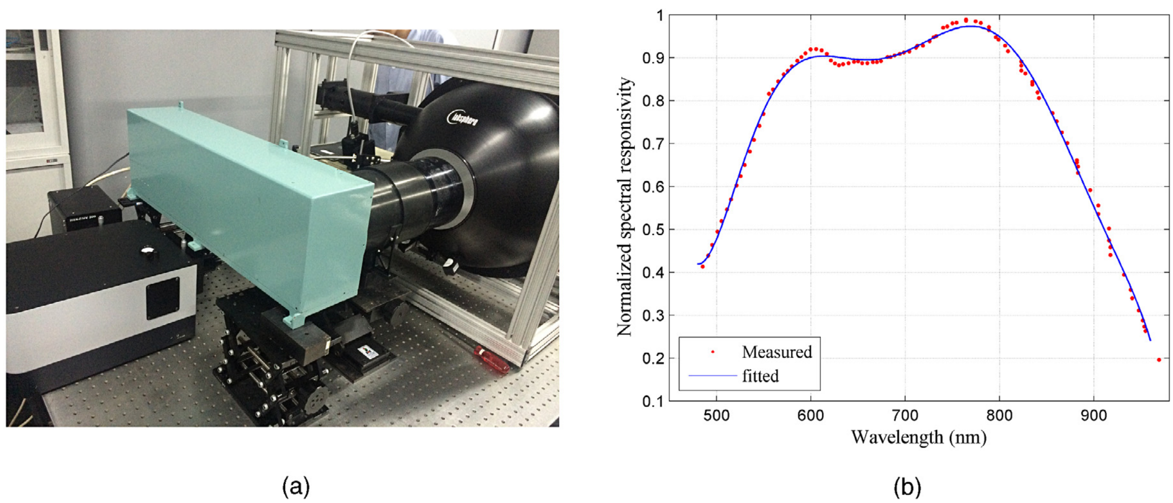

Fig. 12. (a) The data collection of spectral responsivity correction. (b) Normalized spectral responsivity of the CIISP.

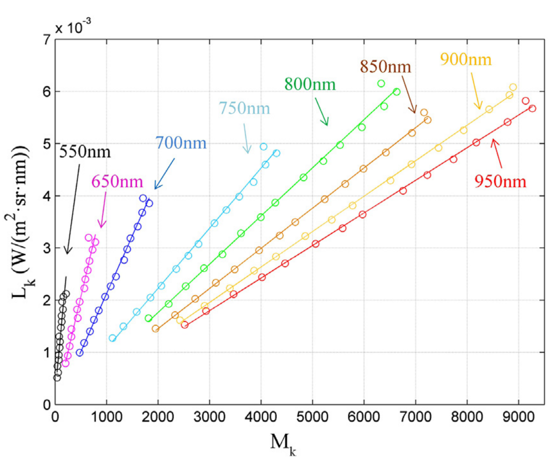

Fig. 13. Fitted result of radiation coefficient calculation with selected wavebands at exposure time of 10 ms.

sample data especially in long wavelength region. Note that the last point deviating from the fitted line can be ignored since the CCD detector was overexposed.

Fig. 14 demonstrates the complete radiometric calibration process of measuring the spectrum of a halogen tungsten lamp. As seen, the red and blue curves in Fig. 14(c) and (d) approximately overlap each other within the middle and long wavelength region of the detecting waveband. The maximum root-mean-square (RMS) error of the calibrated spectrum is $\varepsilon_{max} = 1.88\%$ within the bands $\lambda \geq 600$ nm shown in Fig. 14(c), while it is gradually increased in short wavelength region mainly due to the too weak light intensity within these bands, as well as the low spectral responsivity of CIISP at the edges of the spectral band, which lead to a low signal-to-noise ratio in the reconstructed spectrum.

It should be noted that according to different ways of producing optical path differences for CIISP, it can be classified as temporally-modulated, spatially-modulated, and spatio-temporally modulated mode, respectively [22]. The slight difference in processing of radiometric calibration mainly remains in the link of interferogram uniformity correction. The spatially-modulated mode can obtain complete interferogram of the one-dimensional slit image from single-exposure image, and the other spatial dimension information is acquired by the push-broom of the aircraft along the direction perpendicular to the entrance slit. Therefore, the interferogram uniformity correction can also be performed along the direction of the interference fringe with the same experimental condition and operation. In case of the temporally-modulated mode, the interferogram uniformity correction is more effective and easy to implement, because each collected single-frame image only contains the DN value with a fixed OPD, with no

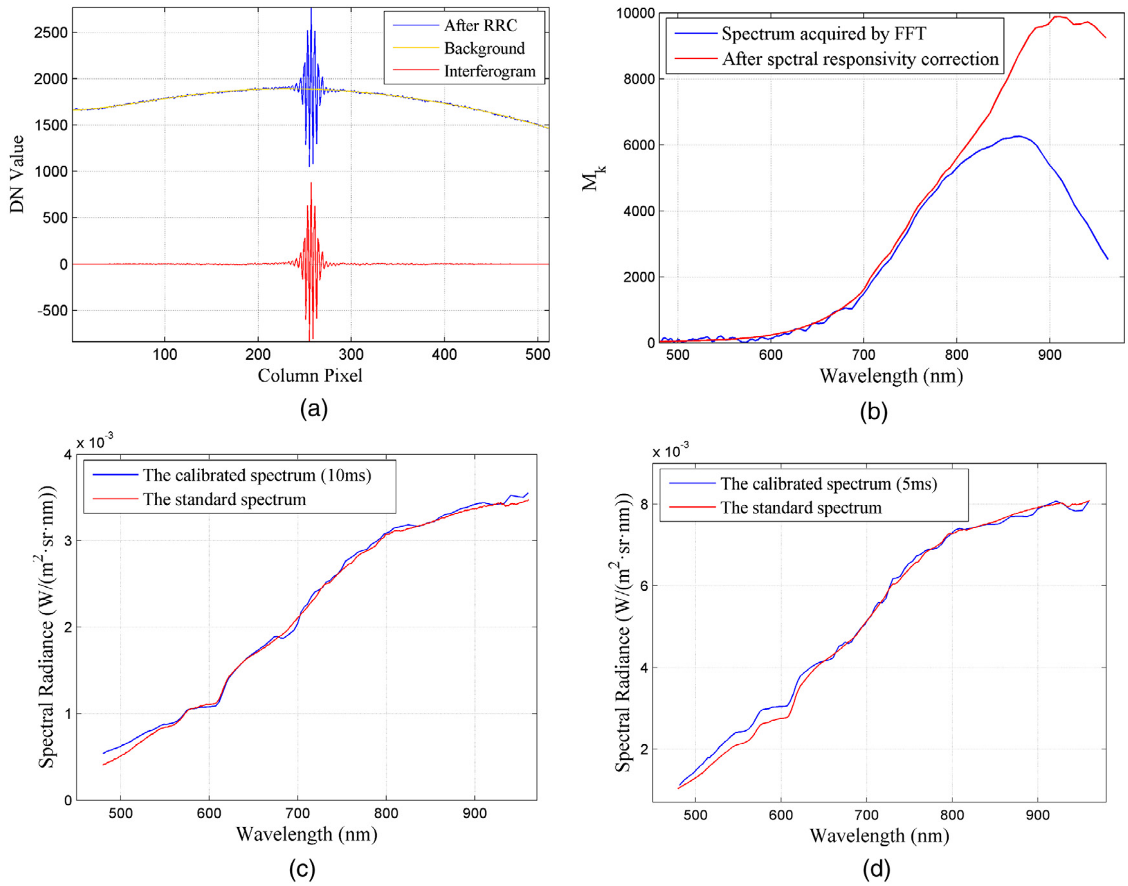

Fig. 14. Radiometric calibration process of measuring the spectrum of the halogen tungsten lamp. (a) Interferogram after relative radiometric calibration. (b) Reconstructed spectrum via spectral responsivity correction. The comparison between the calibrated spectrum and the standard spectrum with exposure time of 10 ms(c) and 5 ms(d), respectively. (For interpretation of the references to color in this figure legend, the reader is referred to the web version of this article.)

bright–dark lines of interference fringe. Therefore, the correction can be performed to the whole single-frame image, rather than along the interference fringe as in the other two modes.

4. Conclusion

In summary, the experimental scheme and processing algorithm of radiometric calibration for the channeled imaging spectropolarimeter were presented. In relative radiometric calibration, the dark current of the CIISP at each exposure time was removed firstly, and then the interferogram uniformity correction was performed along the direction of the fringe by changing the exposure time and input radiance brightness. The response uniformity of pixels in CCD was well improved through the calibration, and the CCD manufacturing defects and the vignetting of the instrument were corrected in a certain degree. By the absolute radiometric calibration, the spectral responsivity was unified at each wavelength, and the functional relation between the standard spectral radiance and the dimensionless reconstructed spectral data was established by using least-squares method. As a result, the maximum RMS error of the calibrated spectrum was approximate $\varepsilon_{max} = 1.88\%$ within the band $\lambda \geq 600$ nm for a halogen tungsten lamp light source, while the error is increased in short wavelength band due to the poor signal-to-noise ratio in the reconstructed spectrum.

Acknowledgments

The work was supported by the Fundamental Research Funds for the Central Universities (Grant No. JB180507, XJS17095) and the Major Program of the National Natural Science Foundation of China (Grant No. 41530422).

References

[1] T. Mu, S. Pacheco, Z. Chen, R. Liang, Snapshot linear-Stokes imaging spectropolarimeter using division-of-focal-plane polarimetry and integral field spectroscopy, Sci. Rep. 7 (2017) 42115–1–10.
[2] D.A. Belyaev, K.B. Yushkov, S.P. Anikin, Y.S. Dobrolenskiy, A. Laskin, Compact acousto-optic imaging spectro-polarimeter for mineralogical investigations in the near infrared, Opt. Express 25 (21) (2017) 25980–25991.
[3] H.J. Hoeijmakers, M.L. Arts, F. Snik, et al., Design trade-off and proof of concept for LOUPE, the Lunar Observatory for Unresolved Polarimetry of Earth, Opt. Express 24 (19) (2016) 21435–21453.
[4] Q. Li, X. He, Y. Wang, et al., Review of spectral imaging technology in biomedical engineering: Achievements and challenges, J. Biomed. Opt. 18 (10) (2013) 100901.
[5] J.S. Tyo, D.L. Goldstein, D.B. Chenault, J.A. Shaw, Review of passive imaging polarimetry for remote sensing applications, Appl. Opt. 45 (22) (2006) 5453–5469.
[6] Qiwei Li, Chunmin Zhang, Tingyu Yan, Yutong Wei, Polarization state demodulation of channeled imaging spectropolarimeter by phase rearrangement calibration method, Opt. Commun. 379 (15) (2016) 54–63.
[7] K. Oka, T. Kato, Spectroscopic polarimetry with a channeled spectrum, Opt. Lett. 24 (21) (1999) 1475–1477.
[8] M.W. Kudenov, N.A. Hagen, E.L. Dereniak, G.R. Gerhart, Fourier transform channeled spectropolarimetry in the MWIR, Opt. Express 15 (20) (2007) 12792–12805.
[9] Y.C. Liu, Y.L. Lo, C.Y. Li, et al., Spectroscopic Stokes polarimetry based on Fourier transform spectrometer, Opt. Commun. 336 (2015) 295–300.
[10] J. Craven, M.W. Kudenov, M. Stapelbroek, E.L. Dereniak, Infrared hyperspectral imaging polarimeter using birefringent prisms, Appl. Opt. 50 (8) (2011) 1170–1185.
[11] J. Li, B. Gao, C. Qi, et al., Tests of a compact static Fourier-transform imaging spectropolarimeter, Opt. Express 22 (11) (2014) 13014–13021.
[12] X. Meng, J. Li, T. Xu, et al., High throughput full Stokes Fourier transform imaging spectropolarimetry, Opt. Express 21 (26) (2013) 32071–32085.
[13] C. Zhang, Q. Li, T. Yan, T. Mu, Y. Wei, High throughput static channeled interference imaging spectropolarimeter based on a Savart polariscope, Opt. Express 24 (20) (2016) 23314–23332.
[14] L.F. Zhang, C.P. Huang, T.X. Wu, F. Zhang, Q. Tong, Laboratory calibration of a field imaging spectrometer system, Sensors 11 (2011) 2408–2425.

[15] C.M. Zhang, L.B. Xiang, B.C. Zhao, X.J. Yuan, A static polarization imaging spectrometer based on a Savart polariscope, Opt. Commun. 203 (2002) 21–26.
[16] A.P. Fossi, Y. Ferrec, N. Roux, O. D'Almeida, N. Guerineau, H. Sauer, Miniature and cooled hyperspectral camera for outdoor surveillance applications in the mid-infrared, Opt. Lett. 41 (2016) 1901–1904.
[17] G. Zhan, K. Oka, T. Ishigaki, N. Baba, Birefringent imaging spectrometer, Appl. Opt. 41 (2002) 734–738.
[18] X.H. Jian, C.M. Zhang, L. Zhang, B.C. Zhao, The data processing of the temporarily and spatially mixed modulated polarization interference imaging spectrometer, Opt. Express 18 (2010) 5674–5680.
[19] J. Craven, M.W. Kudenov, False signature reduction in channeled spectropolarimetry, Opt. Eng. 49 (5) (2010) 053602.
[20] Qiwei Li, Chunmin Zhang, Tingyu Yan, Yutong Wei, Cuncun Tong, Wavelength calibration of an imaging spectrometer based on Savart interferometer, Opt. Commun. 398 (1) (2017) 27–30.
[21] C. Zhang, Q. Li, T. Yan, et al., High throughput static channeled interference imaging spectropolarimeter based on a Savart polariscope, Opt. Express 24 (20) (2016) 23314–23332.
[22] W. Wang, J. Liang, Z. Liang, et al., Design of spatio-temporally modulated static infrared imaging Fourier transform spectrometer, Opt. Lett. 39 (16) (2014) 4911–4914.